Controlled Nitrogen Doping and Film Colorimetrics in Porous TiO_2 Materials Using Plasma Processing

Daniel J. V. Pulsipher,[†] Ina T. Martin,[‡] and Ellen R. Fisher*[,†]

Department of Chemistry, Colorado State University, Fort Collins, Colorado 80523-1872, and National Center for Photovoltaics, National Renewable Energy Laboratory, Golden, Colorado 80401

ABSTRACT Nitrogen doping of TiO_2 films (N:TiO_2) has been shown to improve the visible-light sensitivity of TiO_2, thereby increasing the performance of both photovoltaic and photocatalytic devices. Inductively coupled rf plasmas containing a wide range of nitrogen precursors were used to create nitrogen-doped TiO_2 films. These treatments resulted in anatase-phased materials with as high as 34% nitrogen content. As monitored with high-resolution X-ray photoelectron spectroscopy spectra, the nitrogen binding environments within the films were controlled by varying the plasma processing conditions. XPS peak assignments for multiple N 1s binding environments were made based on high resolution Ti 2p and O 1s XPS spectra, Fourier transform infrared spectroscopy (FTIR) data, and literature N 1s XPS peak assignments. The N:TiO_2 films produced via plasma treatments displayed colors ranging from gray to brown to blue to black, paralleling the N/Ti ratios of the films. Three possible mechanisms to explain the color changes in these materials are presented.

KEYWORDS: titanium dioxide • photocatalysis • photovoltaic • plasma surface modification

INTRODUCTION

Although TiO_2 is widely used in photodevices, its wide bandgap absorbs only a small fraction of the solar spectrum, severely limiting its utility in both photovoltaics and photocatalytic devices. To circumvent this and improve its absorption efficiency, TiO_2 is often modified or sensitized, either directly or indirectly (1). Indirect sensitization can be achieved through the use of dyes or inorganic quantum dots that more efficiently absorb solar radiation, such as in dye-sensitized solar cells. Alternatively, TiO_2 can be more directly sensitized through the modification of its bulk or surface properties, often through the introduction of dopants, a method that is commonly used to improve photocatalytic materials.

A variety of cationic and anionic dopants, including V, Cr, C, F, S, and N have been used to increase the visible light sensitivity of TiO_2 (2). In the past 25 years (3, 4), the photocatalytic functions of nitrogen doped TiO_2 (N:TiO_2) have been widely studied along with its potential use in photovoltaic devices (5−7). Although N:TiO_2 can absorb lower energy solar radiation, the underlying cause of this change remains unclear. One hypothesis, based on the nitrogen chemical environment suggests the visible light sensitivity of N:TiO_2 is the result of N atoms doped into one of two different doping environments, referred to as substitutionally- and interstitially doped N. These two moieties have X-ray photoelectron spectroscopy (XPS) N 1s binding energies of 396 and 400 eV, respectively (8−10). Assignment of XPS N 1s spectral peaks to specific binding environments is often ambiguous and the inclusion of collective analyses of N 1s, Ti 2p, and O 1s binding regions, Fourier transform IR (FTIR) spectroscopy data, and literature peak assignment comparisons increase the reliability of peak assignments. Moreover, this type of comprehensive materials analysis can provide stronger correlations between N:TiO_2 dopant profiles and their respective photosensitivities.

In addition to ambiguities regarding N 1s XPS assignments and the origin of increased visible light sensitivity in N:TiO_2, disagreement also exists over whether introduction of nitrogen changes the material's bandgap. There are several mechanisms that have been proposed to explain this phenomenon. First, some researchers argue that the sensitivity to lower-energy photons is a result of localized states within the bandgap and not to a smaller bandgap (11−13). Serpone and co-workers suggest the amount of dopant required to actually lower the bandgap of N:TiO_2 materials is much greater than commonly reported dopant levels of ≤8% (1, 14, 15). One theoretical study found the bandgap of N:TiO_2 was lowered to 1.80 eV in films with >16.7% N content, with higher concentrations of N lowering the bandgap even further (16). In contrast, other calculations report significantly lower N:TiO_2 bandgaps with as low as 2.8% nitrogen (17). Nevertheless, photocatalytic devices based on N:TiO_2 materials tend to have better performances at low nitrogen doping values, specifically <1% nitrogen (18, 19). An additional consideration is the point at which the material no longer behaves as doped TiO_2, but rather exhibits its own unique properties.

* Corresponding author. E-mail: Ellen.Fisher@colostate.edu.
Received for review March 17, 2010 and accepted May 25, 2010
[†] Colorado State University.
[‡] National Renewable Energy Laboratory.
DOI: 10.1021/am100233j

A second explanation for increased visible-light sensitivity of N:TiO_2 is that it arises from defect states, often described as color centers, oxygen vacancies (O_{vac}), or F-type centers, introduced by the doping process or the dopants themselves (11, 20, 21). Here, F-type centers is used to describe three types of defects found in TiO_2: (a) F-centers, lattice sites where an anion has been replaced by two electrons; (b) F^+-centers, O_{vac} replaced by one electron; and (c) F^{+2}-centers, which are equivalent to O_{vac}. Electrons trapped at F-type centers can be excited by photons, yielding various photoadsorption bands and concomitant color changes. Many nitrogen doping processes involve reducing agents, which favor formation of F-type centers. Indeed, the majority of anionic dopants produce a yellowing effect in TiO_2 materials (8, 22). Additionally, N:TiO_2 reportedly has a lower activation energy for creating O_{vac} than TiO_2 (13, 17), suggesting nitrogen dopants stabilize or allow formation of F-type centers (23).

A third possible explanation for the increased visible response of N:TiO_2 is plasmonic excitations. Plasmons give rise to intense colors in metallic nanoparticles, but are also found in other conductive materials (24). Bulk plasmons can absorb energy according to eq 1

$$\omega_P = \left(\frac{Ne^2}{m^*\varepsilon_0}\right)^{1/2} \quad (1)$$

where ω_p is the plasmon frequency, N is the density of electrons in the valence band, e is the charge of an electron, m^* is the effective mass of the electrons, and ε_0 is the permittivity of free space (25). In addition to bulk plasmons, surface plasmons also absorb photons with their frequency being a fraction of the bulk plasmon frequency. The three mechanisms for increased visible response in N:TiO_2 are, however, difficult to distinguish and may be substantially interrelated.

Here, we characterized the composition and optical properties of TiO_2 films treated in plasma discharges of different N-containing gases, giving rise to N:TiO_2 films with N content of 6−34%. The photoelectric properties of N:TiO_2 are highly dependent on preparation conditions; thus we employed different plasma precursors, parameters, and postplasma treatments to modify our TiO_2 films, resulting in materials with an array of binding environments, as measured with XPS. We have previously used nitrogen-based plasmas to modify the surface of a variety of materials (26−28). Thus, the primary goals of this work were to (1) demonstrate the viability and controllability of plasma processing in creating N:TiO_2 materials and (2) explore potential origins for the resulting electronic properties. The ability to understand and control nitrogen incorporation will ultimately lead to improvements in photocatalytic and photovoltaic devices.

EXPERIMENTAL DETAILS

Porous TiO_2 films were made by calcining a slurry of 5 nm anatase powder, as described previously along with the tubular glass inductively coupled plasma reactor design (29−32). A parametric study was conducted, resulting in the observation that pulsed plasmas with relatively high peak power, short duration time (2−30 min), and low pressures provided the optimal conditions for nitrogen incorporation. Thus, plasmas with nominally 314 ± 1 W of matched, applied 13.56 MHz rf pulsed power having a 70% duty cycle with a 30 ms on time were used. These conditions lead to a plasma density of ∼0.56 W/cm^3 during the on cycle. Unless otherwise noted, gas flow was regulated to maintain a total reactor pressure of 60 ± 5 mTorr by MKS mass flow controllers. Precursor gases were ammonia (Matheson Tri-Gas, product grade), hydrogen (Airgas, product grade), and nitrogen (Airgas, UHP). Pellets of ∼0.4 g of solid urea (Acros, ACS) with 1/2 in. diameters were formed in a pellet press (Carver 4350), and used as sputtering targets positioned ∼1 cm upstream from the sample. Samples were placed parallel to the gas flow in the middle of the plasma coil and were treated for either 2 or 30 min. Films were cleaned prior to all nitrogen doping procedures with a 200 ± 5 mTorr pulsed oxygen (99.9% Airgas) plasma for 2 min at a 70% duty cycle with a 30 ms on time (29).

Table 1. Notation for TiO_2 Film Treatments

film label[a]	plasma gas[b]	time (min)[c]	resting gas[d]
$NH_3(30)/NH_3$	NH_3	30	NH_3
NH_3/NH_3	NH_3	2	NH_3
$NH_3(30)/O_2$	NH_3	30	O_2
NH_3/O_2	NH_3	2	O_2
$H_2,N_2/N_2$	H_2 then N_2	2	N_2
H_2/N_2	H_2	2	N_2
H_2/NH_3	H_2	2	NH_3
N_2/N_2	N_2	2	N_2
annealed			air
urea/NH_3	urea	2	NH_3
untreated TiO_2			

[a] Indicates designation used throughout text for conditions given. [b] Gas used for plasma treatment; for $H_2,N_2/N_2$ treatments, films were treated for 2 min in each plasma environment. [c] Time of initial plasma treatment. [d] Gas environment used post-plasma treatment. Resting time for all films was at least 10 min.

Plasma treatments resulted in substrate temperatures of ≤210 °C during a 2 min treatment and ∼230 °C during a 30 min treatment. These elevated temperatures, along with reactive sites created during plasma treatment, allow chemical reactions to take place even after the discharge is turned off. As a result, the environment in which the substrate is allowed to cool to near room temperature can affect the properties of the films. The plasma-treated TiO_2 films were cooled under the flow of ammonia, hydrogen, nitrogen, and/or argon (Airgas, industrial grade) gases for at least 10 min to explore effects on film composition and optical properties. To identify the different treatments, we have developed a shorthand notation that describes both the plasma treatment and the subsequent cooling environment, Table 1. For example, a TiO_2 sample treated for 2 min with an NH_3 plasma and allowed to cool under an O_2 flow is designated as NH_3/O_2. Likewise, a sample treated in the same manner, but with a 30 min plasma exposure is designated as $NH_3(30)/O_2$. The $H_2,N_2/N_2$ designation represents a TiO_2 film treated in series with a 2 min hydrogen plasma, then a 2 min nitrogen plasma, followed by cooling under N_2. Films designated as "annealed" consist of NH_3/NH_3 films heated under atmosphere in a furnace (Cress Electric, C-101) at 450 °C; annealing time was 30 min unless otherwise stated.

Diffuse reflectance spectra were collected with a Varian Cary500 UV−vis spectrometer with a praying mantis diffuse reflectance attachment. A Teflon standard reference was used.

Table 2. XPS Atomic Concentrations

film label	% N	% Ti	% O	% C	(O + N)/Ti	N/Ti
$NH_3(30)/NH_3$	31.5 ± 2.1	36.4 ± 0.9	31.3 ± 3.0	0.7 ± 0.6	1.73 ± 0.10	0.86 ± 0.04
NH_3/NH_3	21.0 ± 5.2	32.9 ± 2.7	40.9 ± 3.5	5.2 ± 5.2	1.88 ± 0.19	0.64 ± 0.15
$NH_3(30)/O_2$	23.9 ± 1.5	34.4 ± 0.2	40.5 ± 1.7	1.2 ± 1.1	1.87 ± 0.07	0.70 ± 0.04
NH_3/O_2	15.9 ± 0.4	31.6 ± 2.1	47.3 ± 0.4	5.1 ± 2.5	2.00 ± 0.02	0.51 ± 0.03
$H_2,N_2/N_2$	18.1 ± 1.9	32.9 ± 0.6	45.6 ± 2.7	3.5 ± 1.0	1.94 ± 0.10	0.55 ± 0.05
H_2/N_2	9.8 ± 3.2	31.9 ± 0.7	54.6 ± 6.2	3.8 ± 3.3	2.02 ± 0.22	0.31 ± 0.1
H_2/N_2-aged	7.3 ± 3.1	29.7 ± 0.5	58.5 ± 1.9	4.5 ± 1.7	2.22 ± 0.12	0.24 ± 0.10
H_2/NH_3	15.1 ± 2.8	33.3 ± 1.2	46.7 ± 0.6	3.81 ± 2.1	1.86 ± 0.09	0.45 ± 0.08
N_2/N_2	9.2 ± 1.1	31.4 ± 0.3	55.9 ± 1.4	3.5 ± 0.8	2.07 ± 0.06	0.29 ± 0.03
annealed	6.6 ± 1.0	28.9 ± 0.9	62.0 ± 0.4	2.6 ± 0.6	2.37 ± 0.04	0.23 ± 0.04
urea/NH_3	10.0 ± 1.4	23.6 ± 1.2	58.3 ± 3.2	7.3 ± 2.5	2.89 ± 0.15	0.43 ± 0.06
untreated TiO_2		25.8 ± 0.8	62.9 ± 2.9	11.3 ± 3.7	2.44 ± 0.11	

Absorption coefficients of the films were determined from the spectra by use of the Kubelka–Munk function, $F(r)$ (33). Tauc plots were constructed with the assumption of an indirect, allowed bandgap material (34). Tauc bandgap (E_g) values were acquired by plotting $(F(r)h\nu)^{1/2}$ vs $h\nu$ and fitting a line to the linear portion of the graph in the band edge region. When E_g values were calculated, film thickness and substrate effects were not taken into account, thereby potentially introducing some error as the Kubelka–Munk function assumes a smooth and infinitely thick sample (35).

XPS spectra were acquired using a Physical Electronics PE5800 ESCA/AES system using a monochromatic Al K_α X-ray source. A low energy (~1 eV) electron neutralizer was used for charge neutralization. Both survey scans (187.85 eV pass energy, with 0.800 eV/step) and high resolution scans (23.5 eV pass energy, with 0.100 eV/step) were obtained for the TiO_2 films. Spectra were either shifted to the Ti $2p_{3/2}$ peak at 458.6 eV in TiO_2(36), or to the Au $4f_{7/2}$ peak at 84.0 eV by using a cleaned gold O-ring attached to the TiO_2 surface during analysis. Shifting to the gold peak was performed in samples with reduced Ti 2p environments; in unreduced samples the 458.6 Ti $2p_{3/2}$ and 84.0 Au $4f_{7/2}$ eV peaks were aligned. All compositional analysis values were collected from high resolution scans employing a Shirley-type background subtraction in MultiPak V6.1A. Curve fitting was performed using a combination of Gaussian and Lorentzian functions that were allowed to vary in Lorentzian character from 0–25%, with each full width at half-maximum (fwhm) ≤ 2 eV. A 2 kV 3 × 3 mm Ar ion beam from a Physical Electronics ion sputtering gun (11–066) was used to sputter the films to determine the effect on the nitrogen binding environment. Additional compositional analyses were performed to determine the crystallinity of the treated films using X-ray diffraction (XRD) spectroscopy (Scintag X-2 with a Cu X-ray source and Peltier detector). The angle was swept from 5–90° at 0.02°/s. The samples were analyzed in their porous form on fluorinated tin oxide (FTO)-coated glass substrates.

FTIR was used to characterize the chemical environments of treated materials. For each sample, 3–6 films were treated, scraped off the substrate, and pressed into a 1/2 in. diameter pellet. FTIR spectra were collected using a Nicolet Magna 760 spectrometer with a 1 cm^{-1} resolution and an average of 32 scans.

RESULTS

XPS Compositional Analysis. XPS elemental composition data for TiO_2 films treated with different plasmas are listed in Table 2. An array of compositions was obtained, with average %N values ranging from 6.6 to 31.5%. The highest N content is achieved using reductive plasma environments, suggesting NH_3 is more effective than N_2 or urea at promoting N-incorporation. Longer treatment times in NH_3 plasmas also resulted in higher N content, regardless of the post plasma treatment. The films treated using $NH_3(30)/NH_3$, NH_3/NH_3, $H_2,N_2/N_2$, and H_2/NH_3 treatment schemes were all analyzed the same day as the plasma treatment in an attempt to limit the aging/oxidation upon exposure to atmosphere. Over time, the NH_3/NH_3-treated films gain O content as a result of oxidation of less-stable nitrogen or titanium environments and eventually resemble the NH_3/O_2-treated films in atomic composition, Table 2. As anticipated, films exposed to an O_2 environment after plasma treatment contain more oxygen than those cooled under NH_3. The incorporation of nitrogen in H_2 plasma-treated films that were cooled under NH_3 and N_2 demonstrate the reactivity of plasma-reduced TiO_2 films. N_2/N_2 and H_2/N_2-treated films are very similar in % N content. Higher N content in N_2 plasma systems is achieved by first plasma reducing the films and then treating the films in a N_2 plasma, as in $H_2,N_2/N_2$-treated films. Films treated in urea plasmas for 2 and 10 min had similar amounts of nitrogen (data not shown), suggesting that the films saturate quickly.

The thermodynamic stability of TiO_2 over the N–TiO_2 materials studied here is manifested compositionally in post-treatment annealing. NH_3/NH_3-treated samples contain 21.0 ± 2.1% nitrogen, whereas an identical plasma treatment followed by 30 min of annealing results in a dramatic decrease in N content to 6.6 ± 1.0%. This trend also holds for longer annealing times (data not shown), although the N content decreases more slowly with additional annealing time; specifically, after annealing for 120 min ~3% N content remains. In contrast, oxygen incorporation increases from 40.9 ± 3.5% to 62.0 ± 0.4% upon annealing for 30 min.

Table 2 also lists N/Ti ratios for comparison to literature values and (O + N)/Ti ratios, which provide further insight into the Ti coordination in our materials. Specifically, an (O + N)/Ti ratio of 2 corresponds to TiO_2-like coordination of Ti when N and O are treated interchangeably. Similarly, an (O + N)/Ti ratio of 1 more closely resembles the Ti coordination in titanium nitride materials (37). High (O + N)/Ti ratios are indicative of O-terminated surfaces as discussed previously (29). On the basis of these criteria, the (O + N)/Ti ratios

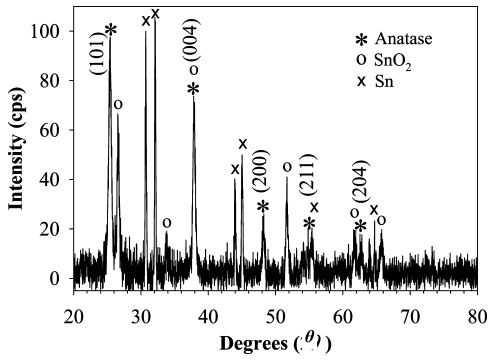

FIGURE 1. XRD data for a $NH_3(30)/NH_3$ film where peaks with index labels correspond to peaks arising from the film. The SnO_2 (110), (101), (200), (211), (310), and (301) peaks and the Sn (200), (101), (220), (211), (301), and (321) peaks arise from the conducting FTO substrate.

suggest our films are more similar to titania or titanium oxynitride than to titanium nitride.

Given the high N content in some of our materials, particularly $NH_3(30)/NH_3$ and $NH_3(30)/O_2$-treated films, we explored the retention of the characteristic crystal structure of anatase TiO_2 using XRD. Figure 1 shows XRD results from a TiO_2 sample subjected to the $NH_3(30)/NH_3$ treatment. All major peaks were assigned to either anatase TiO_2 or the FTO substrate. The film contains no rutile phases, and the absence of any TiN_x or $Ti_{3-\delta}O_4N$ peaks (38) in these data, despite similarities in film colors, suggests that NH_3 plasma treatment does not cause the formation of additional crystalline polymorphs. XRD data from annealed, NH_3/O_2-, and $NH_3(30)/O_2$-treated films parallel those from the $NH_3(30)/NH_3$-treated sample with film peaks corresponding to the anatase structure.

High-resolution N 1s XPS spectra shown in Figure 2 illustrate the effect of processing parameters on films structure. Deconstruction of the spectra yields five distinguishable binding environments, designated as peaks 1−5, with respective binding energies of 396.3 ± 0.2, 397.2 ± 0.2, 398.4 ± 0.2, 399.9 ± 0.3, and 402.4 ± 0.2 eV. Several observations can be made from the spectra in Figure 2. Comparison of panels a and b in Figure 2 show that for NH_3 plasma-treated materials, changing the post-treatment cooling environment from O_2 to NH_3 results in a decrease in the contribution of peak 1 and an increase in the contributions of peaks 2 and 3. These changes are more pronounced with increased plasma treatment time, Figure 2c. The urea plasma-treated sample, Figure 2d, displays a significantly different N 1s spectrum, with the dominant contribution coming from peak 4, along with a small contribution from peak 3. Comparison of panels b and e in Figure 2 show that annealing of the NH_3/NH_3-treated sample yields a dramatic increase in the contribution of peak 5. Figure 2e is representative of spectra for all annealed N-TiO_2 films wherein the incorporated nitrogen is found primarily in the peak 5 binding environment, regardless of its binding environment prior to annealing. Peak 5 does not change upon soaking in water, suggesting it is not a physisorbed species. After ~3 months of aging, the XPS spectrum for annealed films changes somewhat, with peak 5 remaining and peak 4

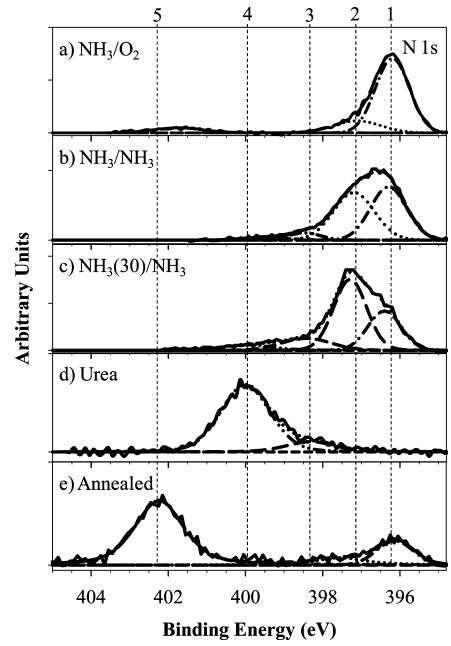

FIGURE 2. High-resolution XPS N 1s spectra with deconstructed fits to the individual components. The vertical dashed lines represent peaks 1−5 located at 396.3 ± 0.2, 397.2 ± 0.2, 398.4 ± 0.2, 399.9 ± 0.3, and 402.4 ± 0.2 eV, respectively.

appearing along with a small N/Ti ratio change from 0.26 to 0.30. When annealed films are subjected to sputtering by 2 kV Ar^+, peak 5 decreases and peaks 1−4 appear, with peak 1 being the most intense after five or more minutes of sputtering. Other plasma treatments, Table 1, result in films with spectra that are comparable to those displayed in Figure 2. Specifically, the spectrum in Figure 2a is representative of those found for N_2/N_2, $NH_3(30)/O_2$, and $H_2,N_2/N_2$ materials, and the spectrum in Figure 2b is representative of those for H_2/N_2- and H_2/NH_3-treated TiO_2.

Additional insight regarding the nitrogen binding in these films can be gained from the Ti 2p binding environments. The Ti $2p_{3/2}$ high-resolution XPS spectra of the N:TiO_2 films are deconvoluted into five peaks, designated as peaks 1−5 with binding energies at 458.55 ± 0.07, 457.38 ± 0.14, 456.19 ± 0.08, 455.24 ± 0.06, and 454.23 ± 0.06 eV, respectively. The relative contributions of these peaks are listed in Table 3 as a function of the different treatments. The air unstable state (peak 5) only appears in films sputtered for >5 min. XPS high-resolution Ti 2p spectra are displayed in Figure 3a−e, with peaks 1−4 appearing as doublets ($2p_{3/2}$ and $2p_{1/2}$) from spin−orbit coupling. Untreated TiO_2 films, urea plasma-treated films, and annealed films have Ti 2p spectra dominated by peak 1, wherein >90 % of the titanium is in the $Ti(-O)_6$ binding environment corresponding to stoichiometric TiO_2. The appearance of peaks 2−4 in Figure 3a−c is, therefore, a reflection of the extent to which treatment affects the chemical environment of the titanium. More specifically, we associate lower-binding energy peaks with reduced titanium. From the data, it is clear that this effect is most pronounced in the case of the $NH_3(30)/NH_3$-treated films, Figure 3c. Additional data found in Table 3 show, for example, H_2/N_2- and H_2/N_2-aged films have spectra resembling that portrayed in Figure 3b. Com-

Table 3. Percent Relative Peak Area for Decomposed XPS Ti $2p_{3/2}$ Peaks[a]

film label	peak 1 (%)	peak 2 (%)	peak 3 (%)	peak 4 (%)	peak 5 (%)	color[b]
sputtered (15 min)	34 ± 6	20 ± <1	16 ± 2	14 ± 3	17 ± 4	black
$NH_3(30)/NH_3$	35 ± 4	24 ± 2	21 ± 4	19 ± 2	–	black
NH_3/NH_3	50 ± 4	25 ± 1	18 ± 1	7 ± 5	<1	dark green
$NH_3(30)/O_2$	52 ± 3	29 ± 2	15 ± 1	3 ± 2	–	dark brown
NH_3/O_2	62 ± 3	33 ± 4	4 ± 1	<1	–	gold
H_2, N_2/N_2	53 ± 6	33 ± 3	11 ± 3	2 ± 3	–	yellow/gold
H_2/N_2	60 ± 24	21 ± 8	12 ± 9	7 ± 8	<1	dark blue
H_2/N_2aged	78 ± 6	14 ± 3	6 ± 2	1 ± 1	<1	gray
N_2/N_2	78 ± 1	16 ± 1	5 ± 1	1 ± 1		slightly yellow
annealed	93 ± 2	7 ± 2	<1			slightly yellow
urea/NH_3	96 ± 2	4 ± 2				white
untreated TiO_2	98 ± <1	2 ± <1				white
literaturessignment	TiO_2	TiO_xN_y	TiO_xN_y	TiN_x	Ti^0, TiN_x	
our assignment	$Ti(-O)_6$	$Ti(-O)_5(-N)_1$	$Ti^{3+}(-O)_5(-N)_1$	$Ti^{3+}(-O)_4(-N)_1(-F^+)_1$	$Ti^{3+}(-N)_3$,Ti^0, $Ti^{3+}-F$	

[a] Peaks 1−5 are located at 458.55 ± 0.07, 457.38 ± 0.14, 456.19 ± 0.08, 455.24 ± 0.06, and 454.23 ± 0.06 eV, respectively. [b] Indicates color film appears upon removal from reactor or upon aging.

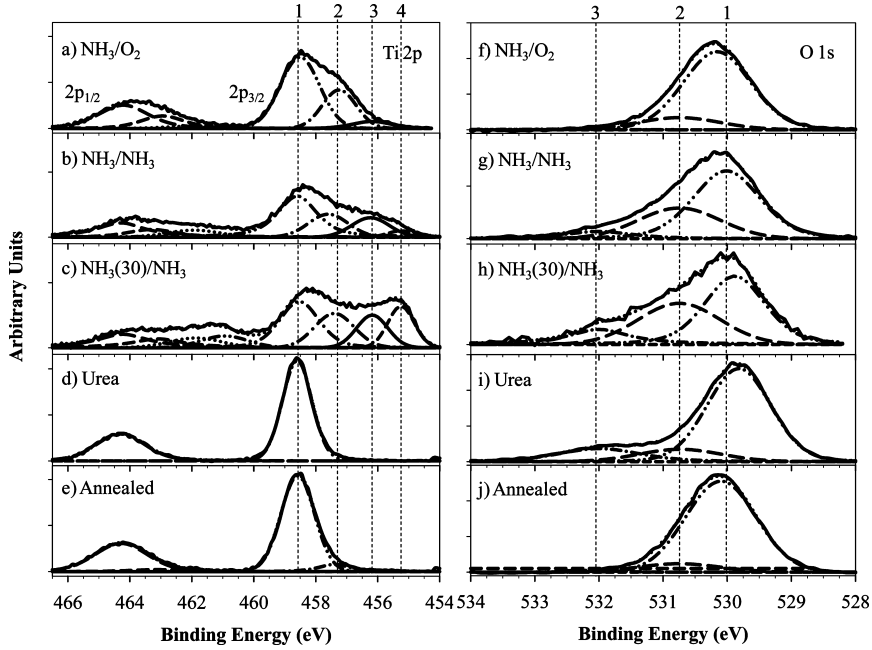

FIGURE 3. High-resolution XPS spectra with deconstructed fits to the individual components for Ti $2p_{1/2}$ and Ti $2p_{3/2}$ peaks (left) with Ti $2p_{3/2}$ peaks 1−4 located at 458.55 ± 0.07, 457.38 ± 0.14, 456.19 ± 0.08, and 455.24 ± 0.06 eV, respectively; and O 1s peaks (right) with peaks 1−3 located at 530.0 ± 0.1, 530.7 ± 0.1, and 532.0 ± 0.1 eV, respectively.

mon literature assignments and our most probable assignments for each Ti 2p binding environment are also listed in Table 3, and discussed further below.

Table 4 explores the relationship between nitrogen and titanium binding environments. Specifically, the %N in peak 1 of the N 1s binding environment corresponds to the %Ti in peak 2 of the Ti 2p binding environment. Similarly, the %N found in peak 2 of the N 1s spectra parallels the amount of Ti found by combining peaks 3 and 4 of the Ti 2p spectra. Ti 2p peaks 3 and 4 can be grouped together due to their association with Ti^{3+} binding environments. In most N:TiO_2 films, the amount of N found in the N 1s peak 1 binding environment is roughly equivalent to the amount of Ti found in the Ti 2p peak 2 binding environment. The exceptions are the $NH_3(30)/O_2$, NH_3/O_2, H_2,N_2/N_2 and N_2/N_2 films. The greater peak 1 %N found in these films is explained by a binding environment where multiple nitrogen atoms are in close proximity to a single titanium atom. A tetrahedral titanium atom bonded to electronegative oxygen atoms is capable of isolating two nitrogen atoms from each other to the extent that their binding environments are not distinguishable from that of one nitrogen atom. This leads to double counting of some of the N 1s peak 1 binding environments that represent the same Ti 2p peak 2 binding environment.

Similar to the high-resolution O 1s spectra discussed in our previous work (29), the O 1s spectra here were decomposed into peaks designated 1−3, Figures 3f−j, with binding energies of 530.0 ± 0.1, 530.7 ± 0.1, and 532.0 ± 0.1 eV, respectively. Peak 1, associated with the $Ti(-O)_6$ binding environment, dominates the spectrum of an untreated TiO_2 film, and as with the Ti 2p spectra, the presence of additional

Table 4. Comparison of N 1s and Ti 2p XPS Atomic Percentages from Each Environment

	N at %		Ti at %			
film label	peak 1	peak 2	peak 2	peak 3 + 4	(N*/Ti*)[a]	color
$NH_3(30)/NH_3$	8.8 ± 0.7	16.4 ± 1.4	9.1 ± 1.1	15.7 ± 1.1	1.0 ± 0.1	black
NH_3/NH_3	10.9 ± 3	8.2 ± 2.2	8.9 ± 0.8	8.6 ± 1.5	1.2 ± 0.3	dark green
$NH_3(30)/O_2$	17.7 ± 1.3	6.2 ± 0.8	10.0 ± 0.7	6.2 ± 0.8	1.8 ± 0.1	dark brown
NH_3/O_2	14.5 ± 0.5	1.3 ± 0.3	10.4 ± 1.4	1.6 ± 0.3	1.4 ± 0	gold
$H_2,N_2/N_2$	13.6 ± 1.5	4.5 ± 0.7	10.9 ± 1	4.3 ± 1.4	1.3 ± 0.1	yellow/gold
H_2/N_2	5.2 ± 1.8	3.6 ± 1.4	6.7 ± 2.6	6.1 ± 3.8	0.8 ± 0.3	dark blue
H_2/N_2aged	4.2 ± 1.8	1.4 ± 0.7	4.2 ± 0.9	2.1 ± 0.7	1.0 ± 0.4	gray
N_2/N_2	7.6 ± 1	1.6 ± 0.3	5.0 ± 0.3	1.9 ± 0.4	1.5 ± 0.2	slightly yellow
annealed	1.3 ± 0.2	0.2 ± 0	2.0 ± 0.6		0.7 ± 0.3	slightly yellow
urea/NH_3	0.3 ± 0		0.9 ± 0.5		0.3 ± 0.5	white
untreated TiO_2			0.5 ± 0.3			white

[a] N* is defined as the N atomic % represented by peak 1 and Ti* is defined as the Ti atomic % represented by peak 2.

peaks indicates modification of the TiO_2 structure. Spectra for $NH_3(30)/NH_3$, NH_3/NH_3, and urea-plasma-modified films show an increase in the O 1s peaks 2 and 3 when compared to annealed and NH_3/O_2 modified films. Although not shown in Figure 3, O 1s spectra of $NH_3(30)/O_2$- and NH_3/O_2-treated films appear experimentally equivalent. O 1s peak assignments are discussed below.

The XPS N 1s spectrum of a 100% urea sample is similar to the N 1s spectrum of our urea plasma-treated films with the majority of the nitrogen existing in peak 4. During a urea plasma treatment, crystalline deposits build up on the reactor walls near the coil region, yet no wall depositions occur in the coil region. This is likely the result of a wall temperature difference. The N content of our urea plasma-treated films decreases when placed in deionized water for several hours, indicating that the nitrogen in this binding environment is relatively water-soluble. To verify that the urea is not simply sputtered onto the TiO_2 films, we heated the films to 150 °C and pumped to 10 mTorr for 60 min, allowing any solid urea to sublime. Subsequent XPS analysis indicates the component at 399.9 eV still dominates the N 1s spectrum, but the total % N decreases significantly. Under these conditions, a 0.2 g urea pellet sublimes in minutes; therefore, solid urea is not redeposited onto the surface of these films.

Further insight into the nitrogen binding environments was pursued through FTIR spectroscopy, Figure 4. Broad peaks at ~3600−3000 cm^{-1}, attributed to the −OH stretch in water absorbed by TiO_2 limit our ability to separate $-OH_x$ from -NH_x absorption peaks. In comparing FTIR spectra of urea and urea-plasma-modified films (Figures 4a and b), however, the FTIR absorbance peaks labeled 1−3 are more distinguishable in the spectrum of the urea pellet. These three absorbance bands (at ~3450, 3350, and 3200 cm^{-1}) are assigned to NH_2, NH, and −NH(C═O) stretching, respectively. The urea plasma-treated TiO_2 films give rise to more intense peaks at 2200, 2050, and 1575 cm^{-1} (absorption bands 4, 5, and 7 in Figure 4), and a much weaker absorption at 1450 cm^{-1} (peak 8). Absorption band 4 (~2200 cm^{-1}) is assigned to N═C═O stretching (39), or −N═C═N functionality; band 5 (~2050 cm^{-1}) is assigned to C≡C or C≡N functionality; band 7 (~1575 cm^{-1}) arises from NH bending,

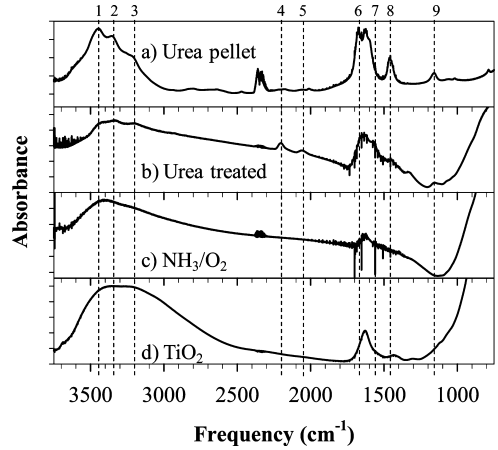

FIGURE 4. FTIR spectra of (a) urea mixed with KBr and (b, c) treated TiO_2 films scraped off of substrates and mixed with KBr. Vertical dashed lines represent peaks 1−9 located at 3450, 3350, 3200, 2100, 1675, 1625, 1575, 1450, and 1150 cm^{-1}, respectively.

again indicating no residual urea precursor in the urea plasma-treated sample; and band 8 (~1450 cm^{-1}) most likely arises from $-CH_2$, or −C−N species. Absorption bands 6 and 9 in spectra for both the urea pellet and the urea plasma-treated TiO_2, panels a and b in Figure 4, were assigned to C═C, C═N, or −N−C═O species and NH_2 rocking or C−O stretching species, respectively. Differences in spectra shown in panels a and b in Figure 4 demonstrate urea is not simply being deposited onto the films. The spectra of the NH_3/NH_3 and $NH_3(30)/NH_3$ films are very similar to the spectrum shown in Figure 4c for the NH_3/O_2 film.

Optical Investigation. A striking aspect of our treated TiO_2 films is the wide range of color changes that occur as the white, untreated samples become shades of yellow, green, brown, blue, and black as a function of both the plasma and the post plasma treatment conditions, Figure 5. Notably, some of the samples change colors as they age, whereas others retain their colors permanently, Table 5. Although a description of these colorimetric changes is somewhat subjective, it does provide additional perspective on the structure and absorption properties of the materials.

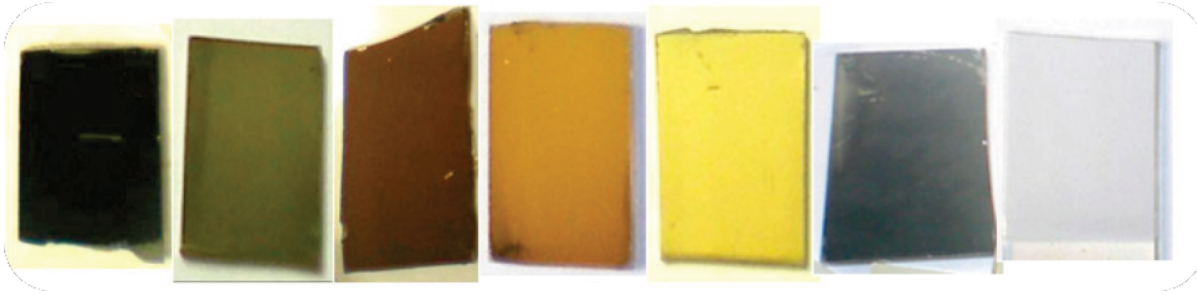

FIGURE 5. Photograph of films depicting the range of colors achieved via different film processing conditions, namely (left to right) NH_3/(30)NH_3, NH_3/NH_3, NH_3/(30)O_2, NH_3/O_2, H_2,N_2/N_2, H_2/N_2-aged, and urea/NH_3-treated films, respectively.

Table 5. Tauc Bandgaps for Modified Films

film label	E_g (eV)[a]	color
NH_3(30)/NH_3		black
NH_3/NH_3		dark green
NH_3(30)/O_2	1.52 ± 0.01	dark brown
NH_3/O_2	2.05 ± 0.09	gold
H_2, N_2/N_2	2.07 ± 0.16	gold/yellow
H_2/N_2		dark blue
H_2/N_2-aged		gray
N_2/N_2	3.10 ± 0.09	slightly yellow
annealed	2.93 ± 0.11	slightly yellow
urea/NH_3	3.33 ± 0.01	white
untreated TiO_2	3.34 ± 0.07	white

[a] Values derived from UV−vis spectra as described in the text.

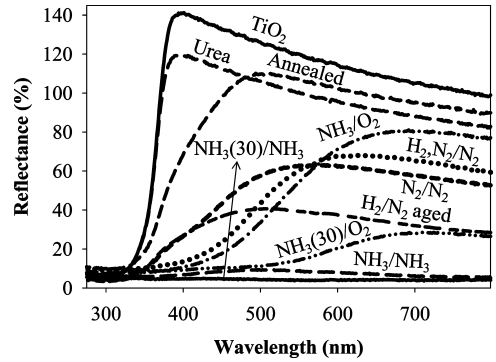

FIGURE 6. Diffuse reflectance UV−vis spectra of TiO_2 films treated with different plasma treatments as labeled.

After a 2 min of NH_3 plasma exposure, the films turn a dark blue color. Depending on the post-plasma treatment, the films turn colors ranging from a dark green to gold. Films allowed to rest under vacuum, argon, nitrogen, or an ammonia flow (NH_3/NH_3) displayed a dark green color and films resting under an oxygen atmosphere (NH_3/O_2) immediately appeared gold. NH_3/NH_3-modified films age considerably upon exposure to atmosphere, reverting to the gold color of the freshly treated NH_3/O_2 films over a period of about one month. NH_3(30)/NH_3 and NH_3(30)/O_2 films become black and brown after treatment. Gold, black, and brown films do not appear to age for a period of at least 5 months. N_2 plasma treatments turn the TiO_2 films a faint yellow color and urea-plasma-modified films (with or without an ammonia carrier gas) appear yellow while still in the reactor under a vacuum, but become white again after being removed from the reactor and exposed to atmosphere.

H_2 plasmas were used to create reactive sites on the TiO_2 surface, which were then allowed to react with a cooling gas, thereby indirectly introducing nitrogen to the film. After 2 min of H_2 plasma exposure, the films appear dark blue; subsequent exposure to NH_3, N_2, O_2, and NO_2 gas flows resulted in additional color changes. Films exposed to NH_3 range from dark blue to dark green colored films which become light green in a few days and ultimately turn gold after a few months. Films cooled under N_2 are dark blue and then age to a gray color. Films exposed to O_2 after a H_2 plasma treatment immediately turned a dull yellow color, and those exposed to N_2 become yellowish-gold in color. XPS spectra of H_2/NH_3 and H_2/N_2-treated films are indistinguishable from those of NH_3/NH_3-treated films, and we assume that the electrical properties of the latter are representative of all of these materials.

To quantify film color changes, we measured absorption spectra using diffuse reflectance UV−vis spectroscopy, Figure 6. The relative intensities of the spectra loosely correlate with the darkness of the films, with the highest and lowest intensities corresponding to white and black films, respectively. Urea plasma-treated films differ from the untreated films only in the slightly lower intensity of the signal. The progressively deeper shades of yellow seen in moving from annealed, to N_2/N_2, and to H_2,N_2/N_2-treated films are more discernible from their diffuse reflectance spectra, Figure 6. Aged H_2/N_2-treated films have a broad and diminished reflectance and NH_3(30)/O_2-treated films have a lower intensity corresponding to their dark brown color. As expected from their dark color, the NH_3/NH_3 and NH_3(30)/NH_3 modified films are extremely low in reflectance.

Tauc bandgaps are determined from the diffuse reflectance spectra by use of the Kubelka−Munk function (34). E_g values, ranging from 1.52 to 3.33 eV, are calculated by fitting data in the linear portion of the absorption band edge of the Tauc plots, Table 5. The indirect bandgap for anatase TiO_2 is ∼3.2 eV (40), although higher experimental bandgaps (3.3−3.5 eV) have been reported (41, 42). The NH_3(30)/O_2-treated films display the lowest accurately determinable E_g. Upon aging, the E_g values for NH_3/NH_3-treated films approach those of NH_3/O_2-treated films (∼2 eV). Poor reflectance signal and/or nonlinearity of the band edge precluded calculation of E_g values for H_2/N_2-aged, NH_3/NH_3, and NH_3(30)/NH_3 films. To explicitly connect the electrical properties of these films with the compositional analysis achieved from XPS, Figure 7 demonstrates the correlation between E_g and

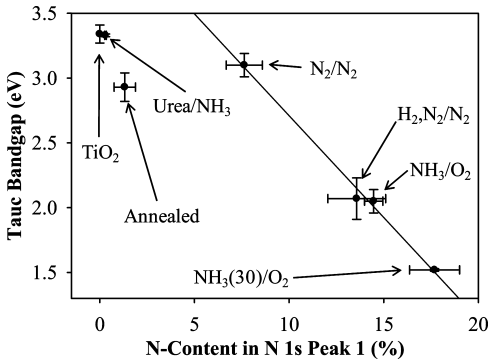

FIGURE 7. Correlation between calculated E_g and amount of nitrogen in the N 1s peak 1 environment for plasma-nitrided films. These data support a localized-nitrogen-dopant light-absorption mechanism.

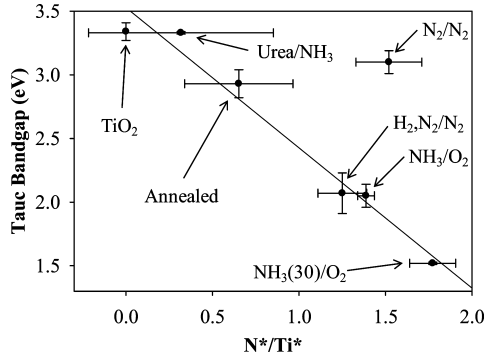

FIGURE 8. Correlations between calculated E_g and N*/Ti* ratios calculated in Table 4. These data support a plasmonic light absorption mechanism.

% N in the N 1s peak 1 environment, and Figure 8 shows E_g values as a function of the N*/Ti* ratios, Table 4. The connection between these data and the underlying mechanisms for nitrogen incorporation are discussed in more detail below.

DISCUSSION

As noted in the Introduction, the primary goals of this work were to explore the use of nitrogen-containing plasmas to controllably produce N:TiO_2 and to examine the underlying mechanisms for doping resulting in increased sensitivity to visible light. Thus, this work has focused on the characterization of our plasma-modified materials utilizing primarily XPS, FTIR, and diffuse reflectance UV−vis spectroscopy to analyze the resulting film properties.

Production and Control of N Doping. N:TiO_2 films produced here contain only anatase domains with the highest N/Ti ratios reported to date of up to 0.90. No evidence of TiN or cubic phased oxynitride (43) crystallinity in either $NH_3(30)/NH_3$- or $NH_3(30)/O_2$-treated films is observed. For crystalline phases other than anatase TiO_2 to form, higher film temperatures would be required than those reached in our plasma treatments. Because XRD completely penetrates the films, anatase-phased TiO_2 could be anywhere in the nanoparticle films and the films with high N content could have amorphous titanium nitride regions. Treatment of TiO_2 in a reducing plasma environment (i.e., in the presence of NH_3 or H_2) yields higher nitrogen loading over a short time. In the literature, N/Ti ratios range from 0.02 to 0.36, with the most common ratio being ∼0.1, corresponding to N:TiO_2 with ∼5% nitrogen (14, 44−49). The highest nitrogen doping for amorphous TiO_2 films is ∼28% (50). Similarly, ≤23% nitrogen was reported in rutile films heated to 800 °C and 49% in TiO_2 nitrided to mostly crystalline TiN at 1100 °C for 5 h (36). Notably, high surface oxidation of our porous films is evident by high surface concentrations of oxygen and by the majority $Ti(-O)_6$ binding environments found in all treated films, Table 3. Additionally, the (O + N)/Ti ratios in Table 2 reflect a titania or titanium oxynitride material.

A major tool used to describe the nitrogen in N:TiO_2 films is high-resolution N 1s XPS spectra as these provide substantial information on the chemical environment (although not specific chemical bonds) of the nitrogen atoms in the film. Peaks 1 and 2 in N 1s spectra for N:TiO_2, Figure 2, are sometimes combined in the literature. Studies of the controlled oxidation of titanium nitride materials suggest, however, that these are two distinct binding environments (51−53). Recently Zhang and co-workers recognized this distinction in high temperature nitridation of TiO_2 and argued that peak 1 was a titanium oxynitride (36). This peak is more often assigned to Ti−N or β-N bonding species which are found in TiN_x materials (54). To clarify the analysis of N 1s data in the present work, we examined the O 1s and Ti 2p spectra of our NH_3/O_2 films, Figure 3. The O 1s spectrum has no features at 532 eV, the region that would be consistent with N−O or oxynitride species (36). By comparison, literature assignments indicate peak 2 in the Ti 2p spectrum, observed in our films, is an oxynitride (54, 55). Given that our XRD data indicate the prevalence of the anatase structure, we have designated peak 2 in the Ti 2p spectrum to a $Ti(-OTi_2)_5(-NTi_2)_1$ or $Ti(-OTi_2)_4(-NTi_2)_2$ environment. Thus, our assignment of peak 1 in the N 1s region to an $N(-TiO_5)_3$ or $N(-TiO_5)_2(-TiO_4N)_1$ binding environment is consistent with the Ti 2p spectrum and with Ti atoms in the Ti^{4+} oxidation state. These Ti 2p (peak 2) and N 1s (peak 1) environments arise from substitutional nitrogen doping where oxygen atoms are replaced with nitrogen atoms. The titanium is in a more reduced environment, yet not enough to formally represent a Ti^{3+} oxidation state.

The N 1s peak 2 has previously been assigned to TiN_x with a binding energy range of 397.1−397.5 eV, depending on the N/Ti ratio (56, 57). Peak 2 constitutes the majority of the N 1s region in spectra of NH_3/NH_3 and $NH_3(30)/NH_3$ films. The significant difference in binding energy for peak 2 in spectra of these two films, Figure 2, results from the change in TiN_x content. The Ti 2p and O 1s XPS spectra for these materials support this N 1s peak assignment. Peak 3 in the Ti 2p spectra has been assigned to an alternative oxynitride species and to Ti^{3+} species in Ti_2O_3 and TiN type materials (55, 58, 59). Additionally the darker color observed has been attributed to the creation of O_{vac} (60, 61), and to the Ti^{3+} to Ti^{4+} optically allowed transition (62). On the basis of the literature assignments, the number of deconstructed Ti 2p peaks, and the stability of the binding environments, peak 3 (Ti 2p) is assigned to $Ti^{3+}(-OTi_2)_5(-NTi_2)_1$. Peak 4 (Ti 2p)

is assigned to a similar environment wherein the Ti^{3+} is bonded to more nitrogen atoms or some of the connecting oxygen atoms are replaced by F-type centers. The increased intensity of the O 1s peaks 2 and 3 in spectra of NH_3(30)/NH_3 films relative to NH_3/NH_3 films could indicate fewer lattice oxygen atoms and more Ti^{3+} states onto which hydroxyl and carboxyl species have absorbed (63, 64). Thus, peak 2 in the N 1s spectrum originates from a titanium nitride-type environment with the titanium in a Ti^{3+} state. Notably, the N−Ti^{3+}−O species appears at a higher N 1s binding energy than N−Ti^{4+}−O as the Ti oxidation state strongly influences binding energy. The chemical structure of this environment probably resembles $N(-Ti^{3+}O_5)_1$-$(-Ti^{4+}O_5)_2$ or a hydrogenated titanium nitride species where the titanium has been reduced to Ti^{3+}.

We also explored the origin of the N 1s signal at 399.9 ± 0.2 eV (peak 4), which appears only in the spectrum of urea plasma-treated films. Peak 4 has been assigned to interstitially doped nitrogen (8, 65), Ti−O−N (14), Ti−N−O (9), Ti−O−N−O (66), NH_x species (67, 68), chemisorbed N_2 species (69), and molecularly absorbed γ-N_2 species (47, 70). The common peak assignment of absorbed γ-N species can be traced to Shinn and co-workers from nitridation of Cr/W wherein they assigned the 400 and 405 eV peaks to well and poorly screened vertically absorbed N_2 molecules, respectively (71). Here, the nitrogen binding environment in H_2/N_2 films were similar to NH_3/NH_3 films where the 399.9 eV peak constituted only a small percentage of the N 1s region (10 ± 1%). Additional C content and higher binding energy peaks in the C 1s XPS spectra of urea plasma-treated films suggest surface oxide or amide-type carbon species. Higher binding energy peaks in the corresponding O 1s spectra indicate carbonyl or NO oxygen species. From the XPS data alone, we cannot discern the origin of the N 1s peak 4. Differences in FTIR spectra obtained from a urea pellet and urea plasma-treated films, Figure 4, permit a more specific assignment of the N 1s peak 4. Using the FTIR assignments given above and the solubility of this environment, peak 4 (399.9 eV) likely arises from weakly bound adsorbates with functional groups that promote water solubility (e.g., −NH−CH═O, −N═C═O, −N═C═N−, and −NH−COH═NH).

Also of interest is the shift toward higher binding energies that accompanies annealing of N:TiO_2 films, yielding a peak at 402.4 ± 0.2 eV (peak 5). Signal in this region has been attributed to interstitially doped nitrogen, NO π^* character, γ-N, molecular N_2, and oxynitride species (14, 70, 72). Upon annealing, the lower binding energy nitrogen environments represented by peaks 1−4 migrate to this higher binding energy environment. Shinn and co-workers observe the opposite phenomenon when their films are annealed in vacuum from 80−1350 K, with nitrogen in the higher N 1s binding energy environment supplying the nitrogen that migrates to a more reduced state. Our data suggest the 402.4 eV binding environment refers to a chemisorbed or trapped species as it does not dissolve in water. The Ti 2p spectra of annealed films show peak 2 accounting for 7 ± 2% of the Ti 2p region, assigned to an intermediate oxynitride species. Given the lack of a N−O signal in the O 1s spectrum, however, it seems more likely that the N 1s signal at 402.4 eV arises from interstitial nitrogen dopants such as trapped N_2, or −N═N− species that are more influenced by Ti^{4+} sites than O^{2-} sites. These species form during the annealing process and then substitutionally order themselves during Ar^+ sputtering.

Possible Optical Mechanisms. Visual changes in TiO_2 that accompany nitrogen doping are closely related to the simultaneous enhancement of the material's photosensitivity. The origin of these color changes remains unclear, with possible mechanisms including lowered bandgaps, intrabandgap localized dopant states, intrabandgap F-type centers, or plasmonic excitations. The first two are supported by the idea that specific XPS N 1s binding environments cause the visible light sensitivity of N:TiO_2 materials. Lower E_g values could, however, result from any of the above-mentioned phenomena. In practice, these explanations are all closely related. Lowered bandgaps can be caused by high concentrations of interbandgap localized dopants or F-type centers; plasmonic energies can be altered by trapping charges at various sites. Although this makes distinguishing between mechanisms difficult, photocatalytic and photovoltaic properties of these materials depend heavily on photoabsorption mechanisms.

When TiO_2 is progressively doped with nitrogen, the nitrogen could initially form localized states within the bandgap of the material. Upon further doping, these states could begin to broaden and overlap, causing absorption of progressively lower energy photons. This phenomena is observed in nitrogen doped diamond where yellow through black diamonds are produced at high nitrogen doping (73). In this case, the amount of a specific nitrogen environment in the films would cause the color changes. Our E_g values for annealed and N_2/N_2-treated films deviate from this argument as two different N 1s binding environment display similar colors. Their E_g values overlap, yet the majority of the incorporated nitrogen is chemically different. This idea cannot be ruled out; however, because the gray, yellow, gold, and brown colors of other films appear to change with the amount of nitrogen in the N 1s peak 1 environment, Table 4 and Figure 7. In fitting the Figure 7 data, both the annealed and urea-treated films were not included in the linear regression analysis because both have significant contributions from other binding environments besides the N 1s peak 1 environment. Thus, the linear trend begins with N_2/N_2-treated films which have the least amount of nitrogen in the N 1s peak 1 environment, and therefore, the least amount of localized nitrogen band broadening.

F-type centers could also cause the optical absorption differences in our N:TiO_2 materials. If defect states such as Ti^{4+}−F^{+2}, Ti^{4+}−F^+, Ti^{4+}−F, and Ti^{3+}−F^+ environments were detectable in the XPS spectra, their concentration would have to be >1000 ppm and F-type centers in concentrations of <1000 ppm can be sufficient to cause color changes. From the Ti 2p peak assignments and relative contribution data, Tables 3 and 4, we infer peak 4 in the Ti 2p spectrum is

associated with F-type centers and nitrogen in the N1s peak 2 environment. The dark films resulting from $NH_3(30)/NH_3$, NH_3/NH_3, H_2/N_2, and $NH_3(30)/O_2$ treatments all contain >3% Ti in the Ti 2p peak 4 environment. If the concentration of F-type centers is high enough, a shallow conduction band could develop; thus, these films could be dark because of high densities of Ti^{3+} sites or F-type centers which are highly interrelated (74). The behavior of NH_3/NH_3 and H_2/NH_3 films over time provides strong indicators for F-type centers. Specifically, peaks 3 and 4 in the Ti 2p spectra decrease in intensity over time, accompanied by color changes from dark green to light green and then to gold with no loss of nitrogen, but a gain in oxygen. All of these data support the conclusion that peak 4 is clearly associated with F-centers, although electron paramagnetic resonance data are needed to definitively detect F^+-centers.

Interestingly, the plasmon frequency of TiN_x films produces similarly colored films depending on the N/Ti ratio. They can appear gray (N/Ti < 1), yellow or gold (N/Ti ≈ 1), and brown (N/Ti > 1) (75−78). These colors are similar to those observed for our $N:TiO_2$ films with the same trend in nitrogen composition. As more nitrogen is added, fewer valence band electrons are available and lower energy plasmons can be created according to eq 1. Available valence electrons could be trapped by localized nitrogen dopants, F-type centers, or other defects. Bendavid and coworkers found that plasmons are not excited at N/Ti ratios as low as 0.34 in films with TiN_x containing <3% oxygen (75). A similar cutoff value of N/Ti could apply to these $N:TiO_2$ materials. Plasmon energies (ω_p) are known to shift linearly from 3.2 to 2.4 eV for TiN_x materials (75, 78); therefore, the concept of smaller E_g values resulting from plasmonic adsorption is probable. Table 4 N*/Ti* ratios are comparable to N/Ti ratios for TiN_x materials and correlate with E_g values, Figure 8. The N_2/N_2-treated films are an obvious outlier in Figure 8, which likely arises from the influence of hydrogen in these systems. Notably, the slightly yellow color of the annealed films does not initially fit the plasmon explanation as these films should have a gray color given the small amount of nitrogen in peak 1 (N 1s) and the concomitantly low N*/Ti* ratio. The majority of the nitrogen in annealed films appears in higher binding environments and likely contributes somewhat to reducing valence band electrons. Thus, the films appear yellow instead of gray. The E_g for urea plasma-treated films is not significantly different than untreated TiO_2, most likely because the nitrogen (largely peak 4) does not significantly affect ω_p. The gray H_2/N_2-aged films also fit this plasmonic absorption mechanism even though E_g was not determined. Although plasmons are a reasonable explanation for the color of these films, further experimentation is needed to confirm the existence of plasmonic excitations.

SUMMARY

Nitrogen doping of mesoporous TiO_2 with a range of N content (6−34%) has been achieved via plasma modification, resulting in low-E_g anatase-phased $N:TiO_2$. The nitrogen environments are controlled by different nitrogen containing precursors as well as post plasma processing. Overall, assignments of the observed XPS N 1s binding environments were elucidated as: peak 1 (396.3 ± 0.2 eV) is substitutional doped $N(-TiO_5)_3$ or $N(-TiO_5)_2(-TiO_4N)_1$ species; peak 2 (397.2 ± 0.2 eV) is attributed to $N(-Ti^{3+}O_5)_1(-Ti^{4+}O_5)_2$ or a hydrogenated hybrid of this species; peak 3 (398.4 ± 0.2 eV) was not assigned as it was not well isolated; peak 4 (399.8 ± 0.2 eV) correlates to absorbed −NH−CH═O, −N═C═O, N═C═N, and/or NH−COH═NH type species; and peak 5 (402.4 ± 0.2 eV), found in annealed films, corresponds to trapped N_2, or −N═N− type species. The $N:TiO_2$ films were gray, yellow, gold, brown, dark green, dark blue, and black. The colors of oxidized films (gray-brown) could be explained both by localized nitrogen dopants and by plasmonic excitations, whereas darker colored films are a result of Ti^{3+} sites and F-type centers. Ultimately, the performance of these materials in solar cell devices and/or in photocatalytic processes is of significant interest. Additional studies utilizing our $N:TiO_2$ materials in photovoltaic and photocatalytic devices is underway.

Acknowledgment. Financial support for this work came from the Center for Revolutionary Solar Photoconversion (CRSP). We also gratefully acknowledge helpful conversations with Prof. C. Michael Elliott and Mr. Joshua M. Stillahn.

REFERENCES AND NOTES

(1) Emeline, A. V.; Kuznetsov, V. N.; Rybchuk, V. K.; Serpone, N. *Int. J. Photoeng.* **2008**, doi:10.1155/2008/258394.
(2) Cui, Y.; Du, H.; Wen, L. S. *J. Mater. Sci. Technol.* **2008**, *24*, 675.
(3) Sato, S. *Chem. Phys. Lett.* **1986**, *123*, 126.
(4) Asahi, R.; Morikawa, T.; Ohwaki, T.; Aoki, K.; Taga, Y. *Science* **2001**, *293*, 269.
(5) Ma, T. L.; Akiyama, M.; Abe, E.; Imai, I. *Nano Lett.* **2005**, *5*, 2543.
(6) Chambers, S. A.; Cheung, S. H.; Shutthanandan, V.; Thevuthasan, S.; Bowman, M. K.; Joly, A. G. *Chem. Phys.* **2007**, *339*, 27.
(7) Cheung, S. H.; Nachimuthu, P.; Joly, A. G.; Engelhard, M. H.; Bowman, M. K.; Chambers, S. A. *Surf. Sci.* **2007**, *601*, 1754.
(8) Fujishima, A.; Zhang, X. T.; Tryk, D. A. *Surf. Sci. Rep.* **2008**, *63*, 515.
(9) Romero-Gomez, P.; Rico, V.; Borras, A.; Barranco, A.; Espinos, J. P.; Cotrino, J.; Gonzalez-Elipe, A. R. *J. Phys. Chem. C* **2009**, *113*, 13341.
(10) Dunnill, C. W. H.; Aiken, Z. A.; Pratten, J.; Wilson, M.; Morgan, D. J.; Parkin, I. P. *J. Photochem. Photobiol., A* **2009**, *207*, 244.
(11) Serpone, N. *J. Phys. Chem. B* **2006**, *110*, 24287.
(12) Kuznetsov, V. N.; Serpone, N. *J. Phys. Chem. C* **2009**, *113*, 15110.
(13) Finazzi, E.; Di Valentin, C.; Selloni, A.; Pacchioni, G. *J. Phys. Chem. C* **2007**, *111*, 9275.
(14) Dong, F.; Zhao, W. R.; Wu, Z. B.; Guo, S. *J. Hazard. Mater.* **2009**, *162*, 763.
(15) Wang, Y. Q.; Yu, X. J.; Sun, D. Z. *J. Hazard. Mater.* **2007**, *144*, 328.
(16) Xue, J. B.; Li, Q.; Liang, W.; Shang, J. K. *J. Wuhan Univ. Technol.* **2008**, *23*, 799.
(17) Chen, Q. L.; Tang, C. Q.; Zheng, G. *Physica B* **2009**, *404*, 1074.
(18) Braun, A.; Akurati, K. K.; Fortunato, G.; Reifler, F. A.; Ritter, A.; Harvey, A. S.; Vital, A.; Graule, T. *J. Phys. Chem. C* **2010**, *114*, 516.
(19) Asahi, R.; Morikawa, T.; Ohwaki, T.; Aoki, K.; Taga, Y. *Science* **2001**, *293*, 269.
(20) Giannakopoulou, T.; Todorova, N.; Osiceanu, P.; Lagoyannis, A.; Vaimakis, T.; Trapalis, C. *Thin Solid Films* **2009**, *517*, 6694.
(21) Tessier, F.; Zollfrank, C.; Travitzky, N.; Windsheimer, H.; Merdrignac-Conanec, O.; Rocherulle, J.; Greil, P. *J. Mater. Sci.* **2009**, *44*, 6110.
(22) Shankar, K.; Basham, J. I.; Allam, N. K.; Varghese, O. K.; Mor, G. K.; Feng, X. J.; Paulose, M.; Seabold, J. A.; Choi, K. S.; Grimes, C. A. *J. Phys. Chem. C* **2009**, *113*, 6327.
(23) Oropeza, F. E.; Harmer, J.; Egdell, R. G.; Palgrave, R. G. *Phys. Chem. Chem. Phys.* **2010**, *12*, 960.

(24) Rhodes, C.; Franzen, S.; Maria, J. P.; Losego, M.; Leonard, D. N.; Laughlin, B.; Duscher, G.; Weibel, S. *J. Appl. Phys.* **2006**, 100.
(25) Maier, S. A. *Plasmonics: Fundamentals and Applications*; Springer: New York, 2007.
(26) Butoi, C. I.; Steen, M. L.; Peers, J. R. D.; Fisher, E. R. *J. Phys. Chem. B* **2001**, *105*, 5957.
(27) Kull, K. R.; Steen, M. L.; Fisher, E. R. *J. Membr. Sci.* **2005**, *246*, 203.
(28) Steen, M. L.; Kull, K. R.; Fisher, E. R. *J. Appl. Phys.* **2002**, *92*, 55.
(29) Pulsipher, D. J. V.; Fisher, E. R. *Surf. Coat. Technol.* **2009**, *203*, 2236.
(30) Mackie, N. M.; Dalleska, N. F.; Castner, D. G.; Fisher, E. R. *Chem. Mater.* **1997**, *9*, 349.
(31) Malkov, G. S.; Martin, I. T.; Schwisow, W. B.; Chandler, J. P.; Wickes, B. T.; Gamble, L. J.; Castner, D. G.; Fisher, E. R. *Plasma Process. Polym.* **2008**, *5*, 129.
(32) Shearer, J. C.; Fisher, M. J.; Hoogeland, D. J.; Fisher, E. R. *Appl. Surf. Sci.* **2010**, *256*, 2081.
(33) Michalow, K. A.; Logvinovich, D.; Weidenkaff, A.; Amberg, M.; Fortunato, G.; Heel, A.; Graule, T.; Rekas, M. *Catal. Today* **2009**, *144*, 7.
(34) Beranek, R.; Kisch, H. *Photochem. Photobiol. Sci.* **2008**, *7*, 40.
(35) Murphy, A. B. *Appl. Opt.* **2007**, *46*, 3133.
(36) Zhang, Z.; Goodall, J. B. M.; Morgan, D. J.; Brown, S.; Clark, R. J. H.; Knowles, J. C.; Mordan, N. J.; Evans, J. R. G.; Carley, A. F.; Bowker, M.; Darr, J. A. *J. Eur. Ceram. Soc.* **2009**, *29*, 2343.
(37) Trenczek-Zajac, A.; Kowalski, K.; Zakrzewska, K.; Radecka, M. *Mater. Res. Bull.* **2009**, *44*, 1547.
(38) Hyett, G.; Green, M. A.; Parkin, I. P. *J. Am. Chem. Soc.* **2007**, *129*, 15541.
(39) Liao, L. F.; Lien, C. F.; Shieh, D. L.; Chen, F. C.; Lin, J. L. *Phys. Chem. Chem. Phys.* **2002**, *4*, 4584.
(40) Tang, H.; Berger, H.; Schmid, P. E.; Levy, F.; Burri, G. *Solid State Commun.* **1993**, *87*, 847.
(41) Sheng, Y. G.; Liang, L. P.; Xu, Y.; Wu, D.; Sun, Y. H. *Opt. Mater.* **2008**, *30*, 1310.
(42) Mahalingam, S.; Edirisinghe, M. J. *Appl. Phys. A: Mater. Sci. Process.* **2007**, *89*, 987.
(43) Drygas, M.; Czosnek, C.; Paine, R. T.; Janik, J. F. *Chem. Mater.* **2006**, *18*, 3122.
(44) Jagadale, T. C.; Takale, S. P.; Sonawane, R. S.; Joshi, H. M.; Patil, S. I.; Kale, B. B.; Ogale, S. B. *J. Phys. Chem. C* **2008**, *112*, 14595.
(45) Qin, H. L.; Gu, G. B.; Liu, S. *C. R. Chim.* **2008**, *11*, 95.
(46) Kitano, M.; Funatsu, K.; Matsuoka, M.; Ueshima, M.; Anpo, M. *J. Phys. Chem. B* **2006**, *110*, 25266.
(47) Parida, K. M.; Naik, B. *J. Colloid Interface Sci.* **2009**, *333*, 269.
(48) Miyauchi, M.; Ikezawa, A.; Tobimatsu, H.; Irie, H.; Hashimoto, K. *Phys. Chem. Chem. Phys.* **2004**, *6*, 865.
(49) Irie, H.; Watanabe, Y.; Hashimoto, K. *J. Phys. Chem. B* **2003**, *107*, 5483.
(50) Song, X. M.; Gopireddy, D.; Takoudis, C. G. *Thin Solid Films* **2008**, *516*, 6330.
(51) Saha, N. C.; Tompkins, H. G. *J. Appl. Phys.* **1992**, *72*, 3072.
(52) Glaser, A.; Surnev, S.; Netzer, F. P.; Fateh, N.; Fontalvo, G. A.; Mitterer, C. *Surf. Sci.* **2007**, *601*, 1153.
(53) Jung, M. J.; Nam, K. H.; Chung, Y. M.; Boo, J. H.; Han, J. G. *Surf. Coat. Technol.* **2003**, *171*, 71.
(54) Chen, C.; Bai, H.; Chang, C. *J. Phys. Chem. C* **2007**, *111*, 15228.
(55) Zorn, G.; Adadi, R.; Brener, R.; Yakoviev, V. A.; Gotman, I.; Gutmanas, E. Y.; Sukenik, C. N. *Chem. Mater.* **2008**, *20*, 5368.
(56) Burrow, B. J.; Morgan, A. E.; Ellwanger, R. C. *J. Vac. Sci. Technol., A* **1986**, *4*, 2463.
(57) Kuznetsov, M. V.; Zhuravlev, M. V.; Shalayeva, E. V.; Gubanov, V. A. *Thin Solid Films* **1992**, *215*, 1.
(58) Kim, Y.; Yoo, B. J.; Vittal, R.; Lee, Y.; Park, N. G.; Kim, K. J. *J. Power Sources* **2008**, *175*, 914.
(59) Takahashi, I.; Payne, D. J.; Palgrave, R. G.; Egdell, R. G. *Chem. Phys. Lett.* **2008**, *454*, 314.
(60) Chae, Y. K.; Mori, S.; Suzuki, M. *Thin Solid Films* **2009**, *517*, 4260.
(61) Liu, H.; Ma, H. T.; Li, X. Z.; Li, W. Z.; Wu, M.; Bao, X. H. *Chemosphere* **2003**, *50*, 39.
(62) Miyaoka, H.; Mizutani, G.; Sano, H.; Omote, M.; Nakatsuji, K.; Komori, F. *Solid State Commun.* **2002**, *123*, 399.
(63) Bullock, E. L.; Patthey, L.; Steinemann, S. G. *Surf. Sci.* **1996**, *352*, 504.
(64) Cao, Y.; Yang, W. S.; Chen, Y. M.; Du, H.; Yue, P. *Appl. Surf. Sci.* **2004**, *236*, 223.
(65) Napoli, F.; Chiesa, M.; Livraghi, S.; Giamello, E.; Agnoli, S.; Granozzi, G.; Pacchioni, G.; Di Valentin, C. *Chem. Phys. Lett.* **2009**, *477*, 135.
(66) Peng, F.; Cai, L. F.; Huang, L.; Yu, H.; Wang, H. J. *J. Phys. Chem. Solids* **2008**, *69*, 1657.
(67) Diwald, O.; Thompson, T. L.; Zubkov, T.; Goralski, E. G.; Walck, S. D.; Yates, J. T. *J. Phys. Chem. B* **2004**, *108*, 6004.
(68) Livraghi, S.; Chierotti, M. R.; Giamello, E.; Magnacca, G.; Paganini, M. C.; Cappelletti, G.; Bianchi, C. L. *J. Phys. Chem. C* **2008**, *112*, 17244.
(69) Chen, D. M.; Jiang, Z. Y.; Geng, J. Q.; Wang, Q.; Yang, D. *Ind. Eng. Chem. Res.* **2007**, *46*, 2741.
(70) Chen, C. C.; Bai, H. L.; Chang, S. M.; Chang, C. L.; Den, W. *J. Nanopart. Res.* **2007**, *9*, 365.
(71) Shinn, N. D.; Tsang, K. L. *J. Vac. Sci. Technol., A* **1991**, *9*, 1558.
(72) Milosev, I.; Strehblow, H. H.; Navinsek, B.; Metikoshukovic, M. *Surf. Interface Anal.* **1995**, *23*, 529.
(73) Nassau, K. *The Physics and Chemistry of Color: The Fifteen Causes of Color*; John Wiley & Sons: New York, 2001.
(74) Li, M.; Hebenstreit, W.; Diebold, U.; Tyryshkin, A. M.; Bowman, M. K.; Dunham, G. G.; Henderson, M. A. *J. Phys. Chem. B* **2000**, *104*, 4944.
(75) Bendavid, A.; Martin, P. J.; Netterfield, R. P.; Kinder, T. J. *Surf. Interface Anal.* **1996**, *24*, 627.
(76) Zhou, Q. G.; Bai, X. D.; Xue, X. Y.; Ling, Y. H.; Chen, X. W.; Xu, J.; Wang, D. R. *J. Alloys Compd.* **2005**, *391*, 141.
(77) Logothetidis, S.; Alexandrou, I.; Papadopoulos, A. *J. Appl. Phys.* **1995**, *77*, 1043.
(78) Roquiny, P.; Bodart, F.; Terwagne, G. *Surf. Coat. Technol.* **1999**, *116*, 278.

AM100233J